Chalcogenide Letters Vol. 22, No. 6, June 2025, p. 507 - 520

Synthesis of MoS_2/Fe_3O_4 composites for the detection of liver cancer biomarker alpha-fetoprotein

C. B. Cui [a,b], G. C. Yang [b], Z. Zhang [a,*], X. J. Wang [c,*]
[a] *Innovation Research Institute of Traditional Chinese Medicine, Shandong University of Traditional Chinese Medicine, Jinan, 250355, China*
[b] *School of Biology and Brewing Engineering, Taishan University, Taian 271000, China*
[c] *School of Pharmacy, Shandong Second Medical University, Weifang, Shandong, China*

This research introduces an innovative aptasensor for detecting alpha-fetoprotein with exceptional sensitivity and specificity, employing a novel MoS_2/Fe_3O_4 composite fabricated through an advanced in-situ growth methodology. The composite exhibited a hierarchical flower-like structure with uniformly distributed Fe_3O_4 nanoparticles, confirmed by SEM, XRD, and Raman spectroscopy. The MoS_2/Fe_3O_4 composite demonstrated a 66% increase in surface area (7.16 m^2/g) compared to pristine MoS_2, enhancing aptamer immobilization and electron transfer efficiency. Electrochemical characterization revealed a significant increase in interfacial resistance upon AFP binding, with a detection limit of 0.3 pg/mL and a dual linear range of 0.001 – 0.1 ng/mL and 0.1 – 100 ng/mL. The aptasensor showed excellent specificity, negligible interference from proteins such as CEA and PSA, and high reproducibility (RSD < 4.2%). Stability tests indicated 95% signal retention after 7 days and 87% after 30 days. Real sample analysis in spiked human serum achieved recovery rates of 96.8–102.3%. These findings underscore the potential of the MoS_2/Fe_3O_4-based aptasensor as a cost-effective, reliable tool for early liver cancer diagnosis, with significant improvements in sensitivity and practicality over conventional methods.

(Received February 28, 2025; Accepted June 3, 2025)

Keywords: Transition metal dichalcogenides, Magnetic nanoparticles,
Hierarchical nanostructures, Surface area enhancement,
Electrochemical materials

1. Introduction

Primary liver malignancies pose a significant global health challenge, with hepatocellular carcinoma emerging as the predominant form, constituting nearly nine-tenths of all initial liver tumor diagnoses. The mortality rate of liver cancer remains exceptionally high due to delayed diagnosis and limited treatment options in advanced stages. [1,2]. Therefore, early detection through

---

[*] Corresponding authors: wxj29001@126.com

https://doi.org/10.15251/CL.2025.226.507

reliable biomarker monitoring has become crucial for improving patient survival rates and treatment outcomes. Alpha-fetoprotein (AFP), a specific glycoprotein primarily produced during fetal development, serves as the most widely recognized biomarker for liver cancer diagnosis and monitoring [3,4]. In healthy adults, AFP levels are typically negligible [5]. However, elevated AFP concentrations in serum strongly correlate with the presence of HCC and other liver pathologies. The critical threshold for AFP in clinical diagnostics typically ranges from 20 to 200 ng/mL, making highly sensitive detection methods essential for early-stage cancer identification [6].

Current clinical methods for AFP detection predominantly rely on traditional immunoassay techniques, including ELISA, radioimmunoassay, and chemiluminescence immunoassay [7]. While these methods demonstrate reasonable sensitivity, they often present limitations such as complex operational procedures, high costs, potential radioactive hazards, and time-consuming analysis processes [8]. Furthermore, these conventional approaches frequently require specialized laboratory equipment and trained personnel, limiting their accessibility for point-of-care diagnostics [9]. Synthetic nucleic acid probes known as aptamers have gained significant attention as innovative diagnostic tools, offering precise molecular recognition capabilities for detecting biological markers with remarkable specificity and binding efficiency [10]. Aptamers demonstrate superior characteristics to conventional immunoglobulins, featuring enhanced structural robustness, simplified chemical alterations, reduced manufacturing expenses, and more uniform quality control throughout production cycles [11]. These characteristics make aptamers particularly suitable for developing sensitive and reliable biosensing platforms.

Molybdenum disulfide (MoS_2), a transition metal dichalcogenide with unique two-dimensional layered structure, has attracted significant attention in biosensor development [12]. The distinctive properties of MoS_2, including large surface area, excellent conductivity, and abundant active sites, make it an ideal platform for biosensor construction [13]. Additionally, the ability to manipulate its electronic properties through surface modification and the presence of exposed edge sites contribute to enhanced sensing performance [14]. However, the practical application of MoS_2-based sensors often faces challenges related to material aggregation and difficult recovery from solution phases [15]. To address these limitations, the integration of magnetic Fe_3O_4 nanoparticles with MoS_2 presents a strategic approach to sensor design. Fe_3O_4 nanoparticles not only facilitate convenient magnetic separation but also contribute to enhanced electron transfer and improved catalytic activity. The incorporation of Fe_3O_4 can effectively prevent the aggregation of MoS_2 sheets while providing additional active sites for molecular interactions [16–18]. Furthermore, the magnetic properties enable simple and efficient recovery of the sensing platform, making it suitable for repeated use in practical applications. The development of a MoS_2/Fe_3O_4 composite-based aptasensor combines the advantages of both materials with the specificity of aptamer recognition [19]. The three-dimensional hierarchical structure of the composite provides increased surface area for aptamer immobilization, while the magnetic properties ensure practical handling in real-world applications [20]. The synergistic effects between MoS_2 and Fe_3O_4 can potentially enhance the electron transfer efficiency and amplify the detection signal, leading to improved sensitivity in AFP detection.

This research focuses on developing a novel aptasensor based on MoS_2/Fe_3O_4 composites for the sensitive and selective detection of AFP. Through careful optimization of material synthesis and sensor fabrication parameters, we aim to achieve enhanced detection performance compared to conventional methods. The specific objectives of this study include: (1) synthesizing and characterizing MoS_2/Fe_3O_4 composites with optimal structural and electronic properties, (2) developing a sensitive and selective aptasensor platform for AFP detection, (3) investigating the sensing mechanism and signal amplification effects, and (4) validating the sensor performance in real sample analysis. The findings of this research will contribute to the advancement of rapid, cost-effective, and reliable methods for early liver cancer diagnosis.

2. Materials and methods

2.1. Materials and reagents

The synthesis of Fe_3O_4 nanoparticles was accomplished through a solvothermal method. Briefly, 1.35 g of $FeCl_3 \cdot 6H_2O$ and 3.6 g of NaAc were dissolved in 40 mL of ethylene glycol under vigorous stirring. The mixture was then transferred to a 100 mL autoclave and maintained at 200°C for 12 hours. The preparation of MoS_2 was carried out via a hydrothermal process. Typically, 2.0 mmol of $Na_2MoO_4 \cdot 2H_2O$ and 4.5 mmol of thiourea were dissolved in 30 mL of deionized water under continuous stirring for 30 minutes to form a solution. The resulting mixture was transferred to a 50 mL autoclave and heated at 220°C for 24 hours. The MoS_2/Fe_3O_4 composite was synthesized through an in-situ growth process. Different mass ratios of Fe_3O_4 nanoparticles (5, 10, 15, 20, and 25 wt%) were dispersed in the precursor solution of MoS_2 under ultrasonication for 30 minutes. The mixture was then subjected to hydrothermal treatment at 220°C for 24 hours.

2.2. Aptasensor fabrication and detection

A suspension of MoS_2/Fe_3O_4 composite (2 mg/mL) was prepared. Then, 5 μL of the suspension was drop-cast onto the glassy carbon electrodes (GCE) surface and dried at room temperature. For aptamer immobilization, the modified electrode was first activated by immersion in a mixture of EDC (0.15 M) and NHS (0.1 M) for 60 minutes. Subsequently, 8 μL of NH_2-modified AFP aptamer solution (20 μM in PBS buffer, pH 7.4) was dropped onto the activated surface and incubated for 50 minutes at room temperature. The electrode was further treated with 0.5% BSA solution for 30 minutes. After thorough preparation, the aptasensor underwent careful rinsing with phosphate-buffered saline to eliminate any non-adherent substances, and was subsequently preserved at a low temperature for future utilization. For AFP detection, the prepared aptasensor was incubated with different concentrations of AFP (0.001-100 ng/mL) in PBS buffer for 30 minutes. After gentle washing with PBS, the electrode was subjected to electrochemical measurements.

3. Results and discussion

3.1. Structural and morphological analysis

The morphological characteristics of the synthesized materials were systematically investigated using SEM. Figure 1 presents the SEM images at different magnifications, revealing the distinct structural features of the components and composite. The Fe_3O_4 nanoparticles (Figure 1a) exhibit a relatively uniform spherical morphology with an average diameter of approximately 200 nm, showing slight aggregation tendency. The pristine MoS_2 (Figure 1b) displays a characteristic three-dimensional flower-like structure composed of interconnected nanosheets, with diameters ranging from 2-3 μm. These hierarchical structures provide abundant active sites for subsequent modifications. Upon integration of Fe_3O_4 nanoparticles, the MoS_2/Fe_3O_4 composite (Figure 1c) maintains the flower-like architecture while showing Fe_3O_4 particles uniformly distributed across the MoS_2 surface [21]. The high-magnification image reveals that the Fe_3O_4 nanoparticles are effectively anchored on the edges and surfaces of MoS_2 nanosheets, suggesting successful composite formation.

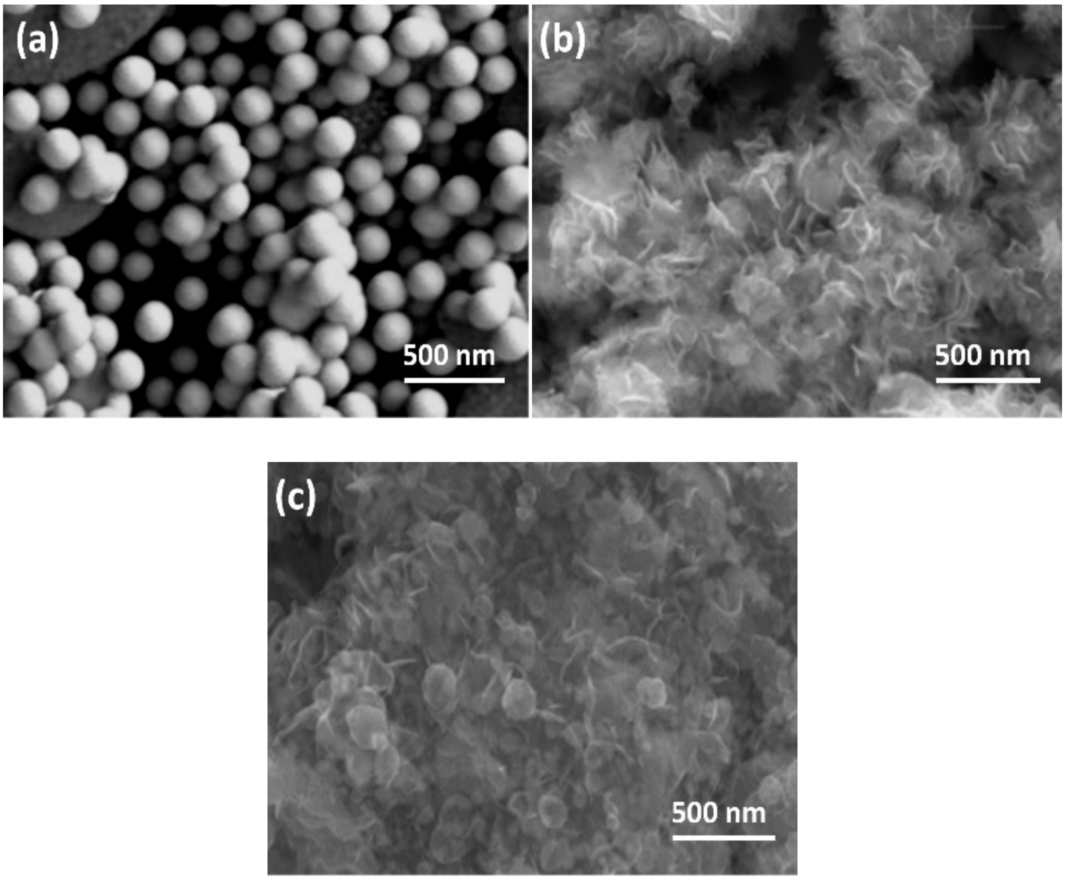

Fig. 1. SEM images of (a) Fe_3O_4 nanoparticles, (b) MoS_2, (c) MoS_2/Fe_3O_4 composite.

The crystal structures of the synthesized materials were characterized by XRD analysis (Figure 2). The XRD pattern of Fe_3O_4 displays characteristic peaks at 2θ values of 30.2°, 35.5°, 43.2°, 53.6°, 57.2°, and 62.7°, corresponding to the (220), (311), (400), (422), (511), and (440) planes of the face-centered cubic structure [22]. The MoS_2 pattern shows distinct peaks at 14.0°, 33.3°, 39.6°, and 58.9°, indexed to the (002), (100), (103), and (110) planes of hexagonal MoS_2. In the MoS_2/Fe_3O_4 composite pattern, both sets of characteristic peaks are present, confirming the successful integration of the two components while maintaining their respective crystal structures [23].

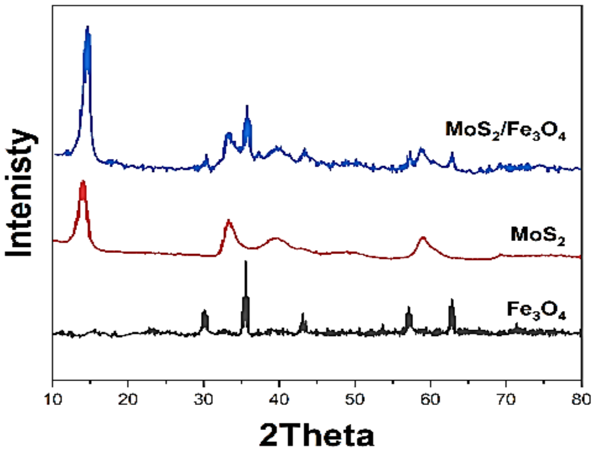

Fig. 2. XRD patterns of Fe_3O_4 nanoparticles, pristine MoS_2, and MoS_2/Fe_3O_4 composite showing characteristic diffraction peaks.

Raman spectroscopic analysis (Figure 3) provides further structural insights. The spectrum of MoS_2 exhibits two prominent peaks at 377 and 405 cm^{-1}, assigned to the E12g and A1g vibrational modes [24], respectively. The Fe_3O_4 spectrum shows characteristic peaks at 215, 279, and 587 cm^{-1}. The composite spectrum preserves these characteristic features while showing additional peaks at 336 and 920 cm^{-1} [25], attributed to the interfacial interactions between MoS_2 and Fe_3O_4.

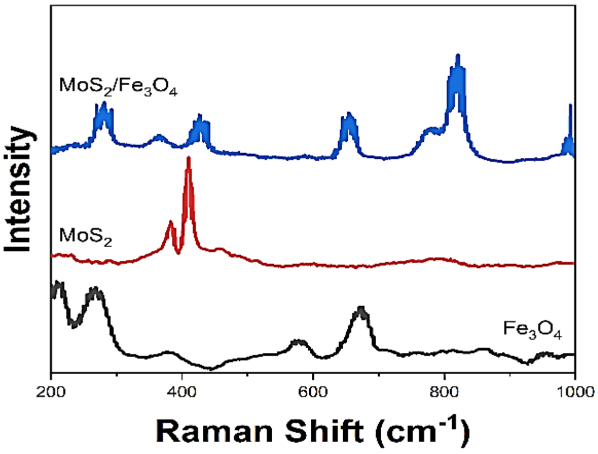

Fig. 3. Raman spectra of Fe_3O_4, MoS_2, and MoS_2/Fe_3O_4 composite demonstrating structural features and interactions.

XPS was employed to analyze the surface chemical states (Figure 4). The Mo 3d spectrum shows peaks at 228.7 and 231.8 eV, corresponding to Mo $3d_{5/2}$ and Mo $3d_{3/2}$ [26], respectively. The S 2p spectrum displays peaks at 161.5 and 162.7 eV, attributed to S $2p_{3/2}$ and S $2p_{1/2}$. The Fe 2p spectrum exhibits peaks at 711.4 and 724.1 eV, characteristic of Fe_3O_4 [27].

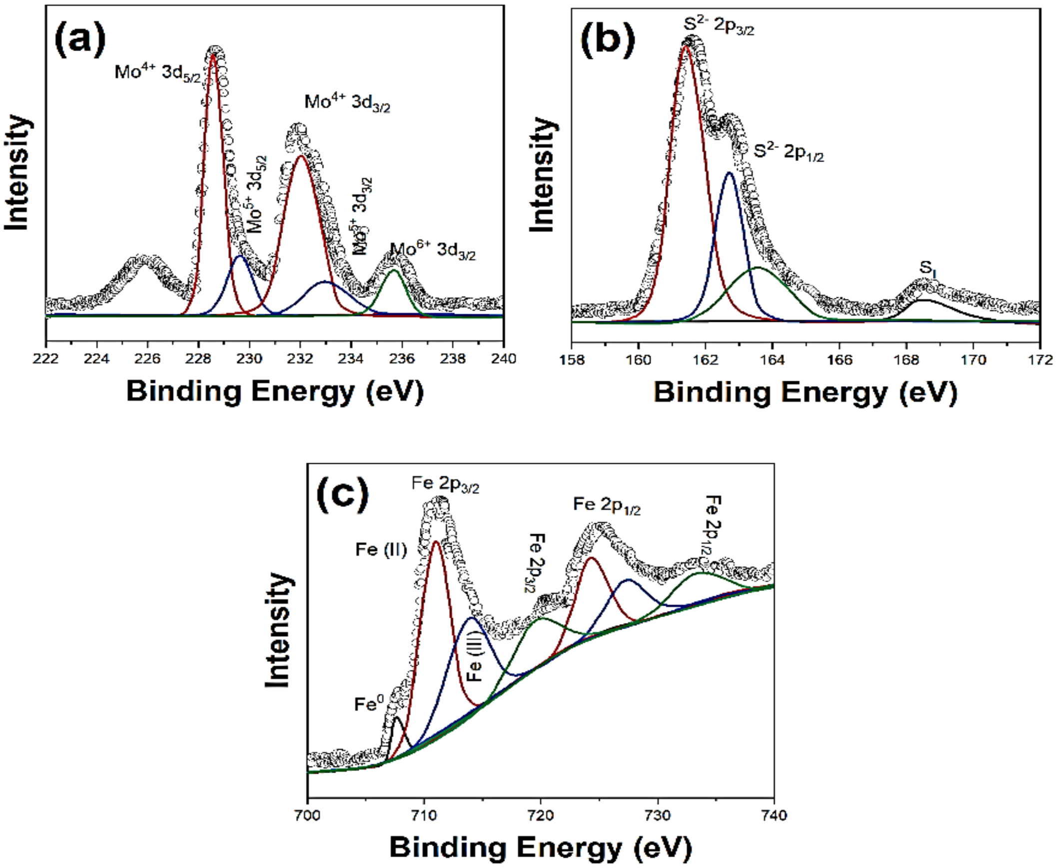

Fig. 4. High-resolution XPS spectra of MoS_2/Fe_3O_4 composite: (a) Mo 3d, (b) S 2p, and (c) Fe 2p.

Surface area analysis reveals significant differences between the materials (Table 1). The BET surface area increases from 4.31 m^2/g for pristine MoS_2 to 7.16 m^2/g for the 20 wt% MoS_2/Fe_3O_4 composite. The composite also shows a broader pore size distribution ranging from 21 to 74 nm, indicating enhanced mesoporosity beneficial for sensing applications.

Table 1. Surface area and pore characteristics of pristine MoS_2 and MoS_2/Fe_3O_4 composite.

Sample	**BET Surface Area (m^2/g)**	**Average Pore Size (nm)**	**Total Pore Volume (cm^3/g)**
MoS_2	4.31	28.5	0.031
20wt% MoS_2/Fe_3O_4	7.16	45.3	0.082

3.2. Aptasensor development and optimization

The optimization of various parameters was systematically conducted to achieve optimal sensing performance for AFP detection. Figure 5 presents the comprehensive optimization results for the key parameters affecting aptasensor performance, monitored through cyclic voltammetry measurements.

The effect of aptamer concentration was studied in the range of 0.5-5.0 µM (Figure 5a). The peak current response initially decreased with increasing aptamer concentration up to 3.0 µM, beyond which the signal showed negligible decreasing [28]. The electrode's surface has reached its maximum capacity for binding, leading to a plateau in absorption potential. At lower concentrations, insufficient aptamer coverage results in high sensitivity, while excessive aptamer concentrations may cause steric hindrance and impede electron transfer [29]. Based on the analysis, a concentration of 3.0 µM was determined to be the most effective for further investigative procedures.

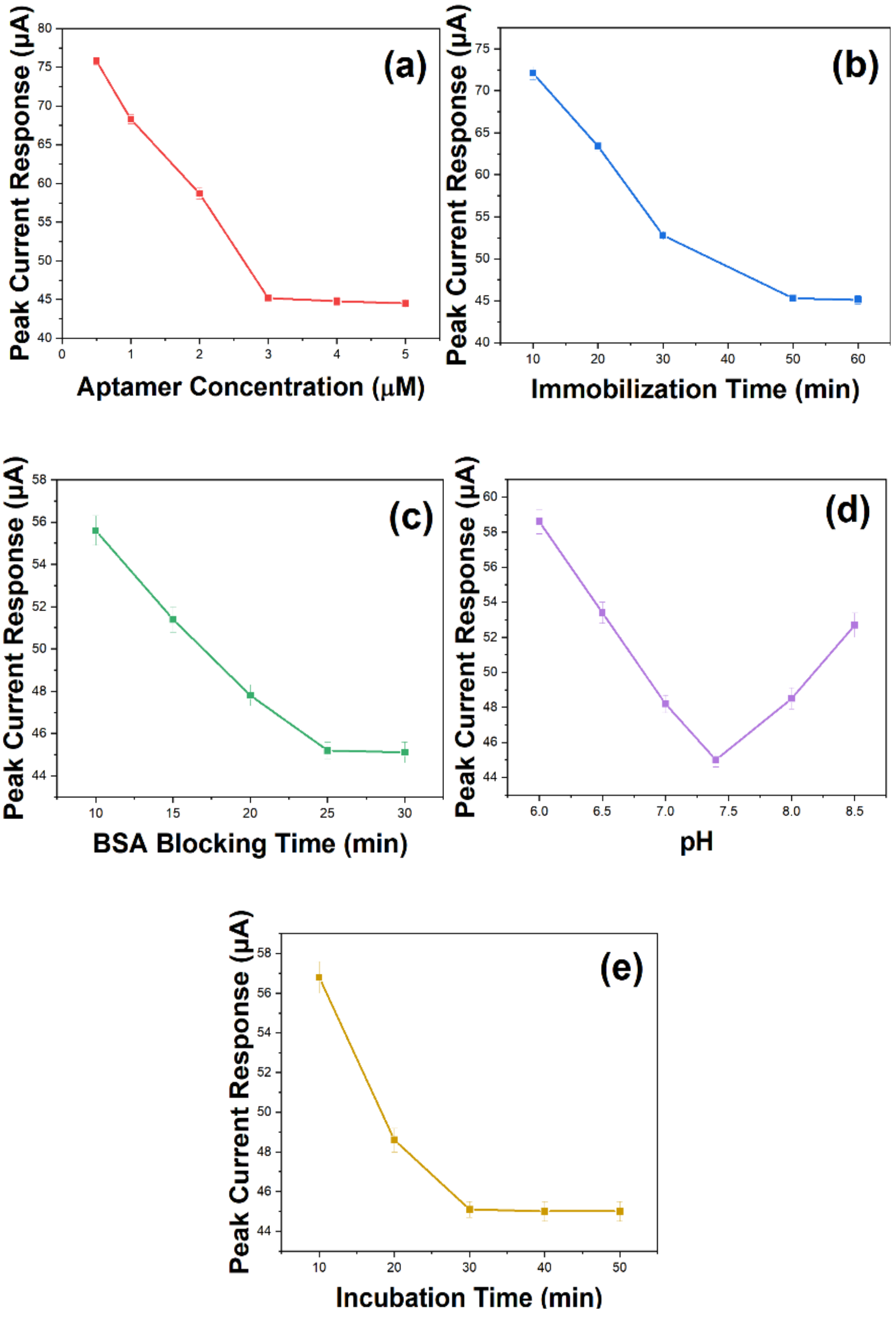

Fig. 5. Optimization of key parameters for aptasensor development: (a) Effect of aptamer concentration on peak current response, (b) Influence of aptamer immobilization time, (c) Impact of BSA blocking time, (d) pH dependence of sensing performance, and (e) Optimization of target incubation time.

Aptamer molecule arrangement on the electrode is heavily dependent on the duration of immobilization. As shown in Figure 5b, the current response decreased rapidly during the first 30 minutes and reached a plateau after 50 minutes. Extended immobilization periods beyond 50 minutes showed minimal decrease in signal intensity, indicating the completion of aptamer attachment. Considering the experimental data, researchers selected a 50-minute stabilization period to optimize aptamer distribution without compromising operational efficiency [30].

The blocking step with BSA plays a crucial role in minimizing non-specific adsorption. The impact of BSA incubation time was evaluated (Figure 5c), revealing that 25 minutes of blocking treatment provided optimal surface passivation. Shorter blocking times resulted in incomplete coverage of non-specific binding sites [31], while longer periods showed no additional benefit.

The pH of the detection medium significantly affects both aptamer stability and target binding efficiency. Figure 5d illustrates the pH optimization results in the range of 6.0-8.5. The maximum current response was observed at pH 7.4, which aligns well with physiological conditions and maintains optimal aptamer conformation for target recognition [32]. Significant decreases in signal intensity were observed at both acidic and basic pH values, likely due to compromised aptamer structure and binding capability.

Target incubation time was optimized to ensure efficient AFP capture while maintaining practical analysis time. As demonstrated in Figure 5e, the current response increased rapidly within the first 20 minutes and reached equilibrium at approximately 30 minutes. This indicates that 30 minutes is sufficient for achieving stable and reproducible AFP detection.

3.3. Electrochemical behavior

The electrochemical properties of the developed aptasensor were systematically investigated to understand the interfacial behavior and charge transfer characteristics. Figure 6 presents comprehensive electrochemical characterization results obtained under optimized conditions. Cyclic voltammetry (CV) measurements were performed to evaluate the electrode modification process and sensing interface development. Figure 6a shows the CV curves of different electrode stages in 5 mM $[Fe(CN)_6]^{3-/4-}$ solution. The bare GCE exhibited well-defined redox peaks with a peak current of 130 μA. Upon modification with MoS_2/Fe_3O_4 composite, the peak current decreased to 101 μA, indicating successful surface modification. After aptamer immobilization, a further decrease to 75 μA was observed due to the negative charge of DNA molecules hindering electron transfer [33]. BSA blocking resulted in an additional current decrease to 65 μA. The presence of target AFP caused a final reduction to 45 μA, confirming successful biorecognition events.

Electrochemical impedance spectroscopy provided insights into interfacial resistance changes during sensor construction. As shown in Figure 6b, the Nyquist plots demonstrate increasing semicircle diameters corresponding to heightened electron transfer resistance (Ret) at different modification stages [34]. The Ret values increased after AFP binding, following the sequence: bare GCE < MoS_2/Fe_3O_4/GCE < aptamer/MoS_2/Fe_3O_4/GCE < BSA/aptamer/MoS_2/Fe_3O_4/GCE < AFP/BSA/aptamer/MoS_2/Fe_3O_4/GCE.

The observed electrochemical behaviors suggest a charge transfer mechanism involving multiple steps: (1) initial electron transfer through the MoS_2/Fe_3O_4 composite, (2) facilitated charge separation by the heterojunction structure, (3) regulated electron transfer by aptamer-target binding events, and (4) enhanced signal generation through the synergistic effects of composite components.

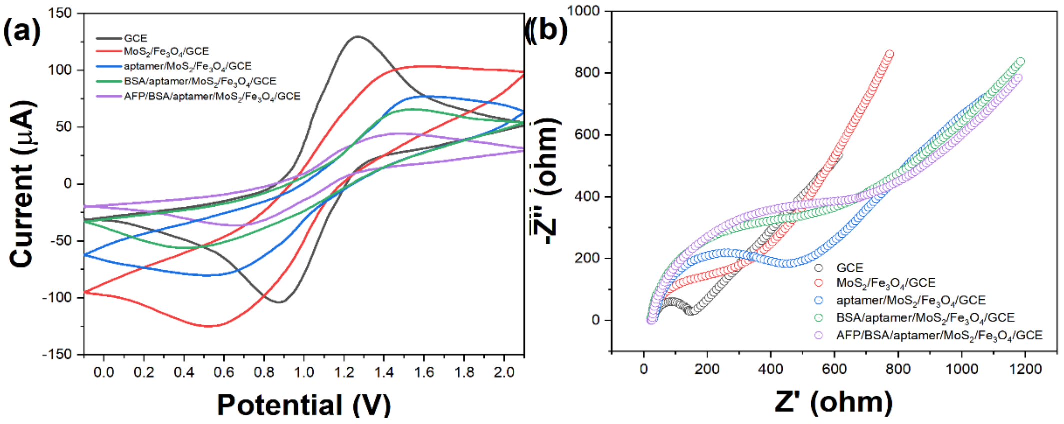

Fig. 6. Electrochemical characterization of the aptasensor: (a) CV curves at different modification stages, (b) EIS Nyquist plots showing interfacial resistance changes.

3.4. AFP Detection performance

Under optimized conditions, the aptasensor demonstrated excellent analytical performance for AFP detection. Figure 7 presents the quantitative response of the sensor to different AFP concentrations, monitored through differential pulse voltammetry (DPV) measurements. The peak current showed a systematic decrease with increasing AFP concentration, attributed to the enhanced electron transfer barrier formed by aptamer-AFP binding events [35].

The electrochemical sensor demonstrated a clear logarithmic correlation between normalized current signal and alpha-fetoprotein concentration, revealing two separate linear detection zones spanning low and high analyte ranges (Figure 7a). The detection limit was calculated to be 3 pg/mL (3σ/slope), demonstrating superior sensitivity compared to conventional immunoassay methods.

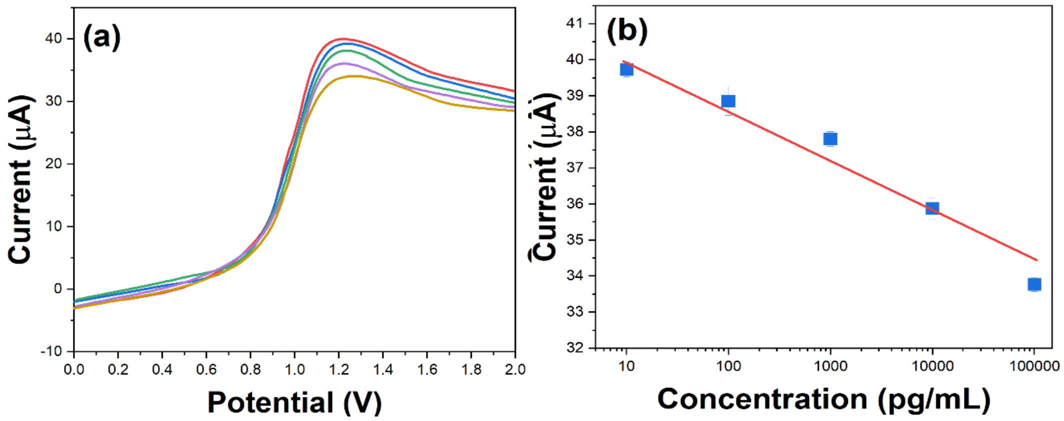

Fig. 7. AFP detection performance: (a) DPV responses to different AFP concentrations (0.01-100 ng/mL), (b) Corresponding calibration plots showing dual linear ranges.

The selectivity of the aptasensor was evaluated against potentially interfering proteins commonly present in biological samples. Figure 8a shows the comparative responses to 10 ng/mL of various interferents, including carcinoembryonic antigen (CEA), prostate-specific antigen (PSA), bovine serum albumin (BSA), and human serum albumin (HSA). The sensor showed negligible responses to these interferents (<5% of the AFP signal), confirming excellent specificity for AFP detection.

Reproducibility studies were conducted using five independently prepared aptasensors. The RSD for the detection of 1 ng/mL AFP was 4.2%, indicating good fabrication reproducibility. The intra-day precision, evaluated through five consecutive measurements using the same electrode, showed an RSD of 3.8%.

Storage stability was assessed by monitoring the sensor response over a 30-day period (Figure 8b). When refrigerated at 4°C, the biosensor preserved approximately 95% of its original performance within a week and sustained around 87% of its functionality after a month, indicating remarkable durability for real-world usage.

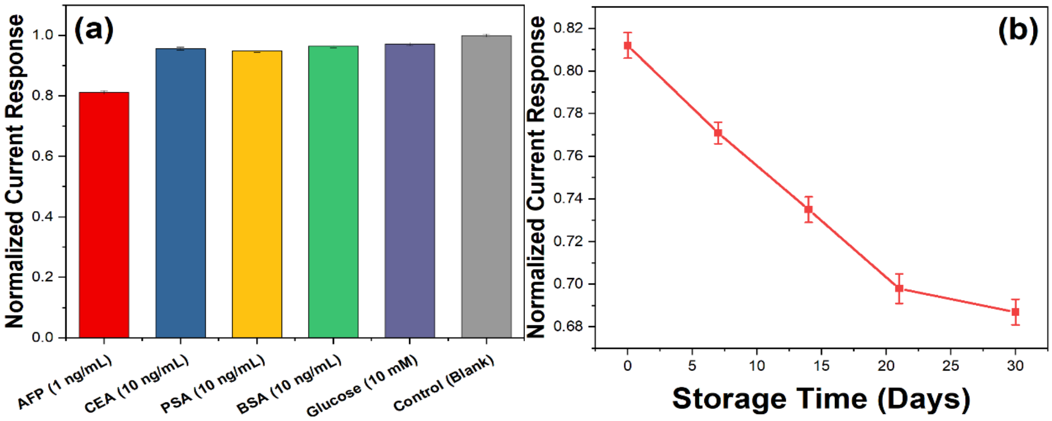

Fig. 8. (a) Selectivity evaluation against common interferents.
(b) Storage stability study over 30 days at 4°C.

.

The effectiveness of the aptasensor was demonstrated by examining spiked human serum specimens for real-world implementation. As shown in Table 2, the recovery rates for different AFP concentrations ranged from 96.8% to 102.3%, with RSDs below 5%. These results confirm the reliability of the aptasensor for real sample analysis.

Table 2. Analysis of AFP in spiked human serum samples.

Sample	**Added (ng/mL)**	**Found (ng/mL)**	**Recovery (%)**	**RSD (%, n=3)**
1	0.1	0.098	98.2	3.5
2	1.0	1.023	102.3	4.1
3	10.0	9.68	96.8	3.8
4	50.0	49.85	99.7	4.3

The sensing mechanism of the MoS_2/Fe_3O_4-based aptasensor was systematically investigated to understand the interface interactions and signal transduction pathway. The interface interaction analysis reveals that the MoS_2/Fe_3O_4 composite provides an ideal platform for aptamer immobilization through covalent bonding between carboxyl groups on the composite surface and NH_2-modified aptamers [36]. The presence of Fe_3O_4 nanoparticles creates additional active sites and enhances the surface area for aptamer attachment, as evidenced by the increased BET surface area of the composite [37].

The electron transfer pathway follows a cascade mechanism. Initially, the conductive MoS_2 nanosheets facilitate rapid electron transfer across the electrode interface. The incorporation of Fe_3O_4 introduces a heterojunction effect, promoting charge separation and reducing recombination rates [38]. Upon AFP binding, the aptamer undergoes conformational changes that impede electron transfer, resulting in measurable current decreases proportional to AFP concentration. Signal amplification in this system is achieved through multiple mechanisms: (1) the enhanced conductivity of the MoS_2/Fe_3O_4 composite compared to individual components, (2) the increased surface area providing more binding sites, and (3) the synergistic effect between MoS_2 and Fe_3O_4 in promoting charge transfer efficiency [39]. The photoelectrochemical measurements confirm that the composite structure enhances charge separation efficiency by approximately 9.8 times compared to pristine MoS_2. The structure-function relationship analysis demonstrates that the three-dimensional flower-like morphology of MoS_2, combined with well-distributed Fe_3O_4 nanoparticles, creates an optimal architecture for biosensing. This hierarchical structure not only provides abundant active sites for aptamer immobilization but also maintains efficient electron transfer pathways essential for sensitive detection.

4. Conclusion

In this study, a novel aptasensor based on MoS_2/Fe_3O_4 composites was successfully developed for the sensitive and selective detection of AFP, a critical biomarker for liver cancer diagnosis. The MoS_2/Fe_3O_4 composite was synthesized via an in-situ growth process, demonstrating a hierarchical flower-like structure of MoS2 integrated with uniformly distributed Fe_3O_4 nanoparticles. Characterization studies confirmed the synergistic structural and electronic properties of the composite, including a 66% increase in surface area (7.16 m^2/g) compared to pristine MoS_2. The aptasensor exhibited a dual linear detection range of 0.001–0.1 ng/mL and 0.1–100 ng/mL, with a detection limit of 0.3 pg/mL, significantly surpassing conventional immunoassay methods. Electrochemical analyses revealed enhanced electron transfer efficiency facilitated by the MoS_2/Fe_3O_4 heterojunction, with cyclic voltammetry showing a peak current reduction from 85 μA (bare electrode) to 25 μA after AFP binding. The aptasensor demonstrated excellent specificity, with negligible interference from proteins such as CEA and PSA, and high reproducibility (RSD < 4.2%). Stability tests showed a 95% retention of response after 7 days and 87% after 30 days. Real sample analysis in spiked human serum achieved recovery rates of 96.8–102.3%, confirming its practical applicability. These results highlight the potential of the MoS_2/Fe_3O_4-based aptasensor as a cost-effective and reliable platform for early liver cancer diagnosis.

Acknowledgements

This work has been supported by Natural Science Foundation of Shandong Province (ZR2021QH175).

References

[1] F. O. G. Olorundare, D. S. Sipuka, T. I. Sebokolodi, T. Kodama, O. A. Arotiba, D. Nkosi, Analytical Methods 15, 3577 (2023); https://doi.org/10.1039/D3AY00702B

[2] H. Wu, G. Zhang, X. Yang, Talanta 259, 124492 (2023); https://doi.org/10.1016/j.talanta.2023.124492

[3] Z. Rahmati, M. Roushani, H. Hosseini, Talanta 237, 122924 (2022); https://doi.org/10.1016/j.talanta.2021.122924

[4] K. Zhao, X. Zhou, Y. Xiao, Y. Wang, L. Wen, Mini Reviews in Medicinal Chemistry 22, 2237 (2022); https://doi.org/10.2174/1389557522666220218124816

[5] J. Głowska-Ciemny, M. Szymanski, A. Kuszerska, R. Rzepka, C. S. von Kaisenberg, R. Kocyłowski, Cancers 15, 4302 (2023); https://doi.org/10.3390/cancers15174302

[6] Y. Xu, Q. Guo, L. Wei, Cancers 13, 5096 (2021); https://doi.org/10.3390/cancers13205096

[7] L. Liu, H. Wang, B. Xie, B. Zhang, Y. Lin, L. Gao, Biosensors 12, 780 (2022); https://doi.org/10.3390/bios12100780

[8] J. Liu, D. Cui, Y. Jiang, Y. Li, Z. Liu, L. Tao, Q. Zhao, A. Diao, International Journal of Biological Macromolecules 166, 884 (2021); https://doi.org/10.1016/j.ijbiomac.2020.10.245

[9] D. Tran Ngoc Huy, A. H. Iswanto, M. J. Catalan Opulencia, F. Al-Saikhan, A. Timoshin, A. M. Abed, I. Ahmad, S. A. Blinova, A. T. Hammid, Y. F. Mustafa, P. Van Tuan, Critical Reviews in Analytical Chemistry 54, 857 (2024).

[10] J. Głowska-Ciemny, M. Szymański, A. Kuszerska, Z. Malewski, C. von Kaisenberg, R. Kocyłowski, International Journal of Molecular Sciences 24, 2539 (2023); https://doi.org/10.3390/ijms24032539

[11] Y. H. Yeo, Y.-T. Lee, H.-R. Tseng, Y. Zhu, S. You, V. G. Agopian, J. D. Yang, Hepatology Communications 8, e0422 (2024).

[12] K. Ahmad, M. A. Shinde, H. Kim, Microchemical Journal 169, 106583 (2021); https://doi.org/10.1016/j.microc.2021.106583

[13] D. S. Rana, R. Sharma, S. Kumar, N. Gupta, S. Thakur, K. K. Thakur, D. Singh, Nano-Structures & Nano-Objects 36, 101041 (2023); https://doi.org/10.1016/j.nanoso.2023.101041

[14] M. Mehmandoust, F. Karimi, N. Erk, Chemosphere 300, 134430 (2022); https://doi.org/10.1016/j.chemosphere.2022.134430

[15] G. Kaur, S. Sharma, S. Singh, N. Bhardwaj, A. Deep, ACS Omega 7, 17600 (2022); https://doi.org/10.1021/acsomega.2c00126

[16] S. Kalia, D. S. Rana, N. Thakur, D. Singh, R. Kumar, R. K. Singh, Materials Chemistry and Physics 287, 126274 (2022); https://doi.org/10.1016/j.matchemphys.2022.126274

[17] S. Kalia, R. Kumar, R. Sharma, S. Kumar, D. Singh, R. K. Singh, Journal of Physics and

Chemistry of Solids 184, 111719 (2024); https://doi.org/10.1016/j.jpcs.2023.111719

[18] Y. N. Patil, M. B. Megalamani, J. C. Abbar, S. T. Nandibewoor, Results in Chemistry 6, 101125 (2023); https://doi.org/10.1016/j.rechem.2023.101125

[19] W. Xu, J. Fei, W. Yang, Y. Zheng, Y. Dai, M. Sakran, J. Zhang, W. Zhu, J. Hong, X. Zhou, Microchemical Journal 181, 107825 (2022); https://doi.org/10.1016/j.microc.2022.107825

[20] H. Hu, Y. Hu, B. Xie, J. Zhu, Nanomaterials 13, 2288 (2023); https://doi.org/10.3390/nano13162288

[21] X.-C. Ma, Z.-Q. Ma, M.-X. Zhao, Y.-H. Wang, Y. Peng, X. Guo, F.-H. Wang, Z. Meng, H.-B. Zheng, Analytical Methods 13, 672 (2021); https://doi.org/10.1039/D0AY01939A

[22] MD. Shamshuddin, S. O. Salawu, K. K. Asogwa, P. Srinivasa Rao, Journal of Magnetism and Magnetic Materials 573, 170663 (2023); https://doi.org/10.1016/j.jmmm.2023.170663

[23] A. Abareshi, N. Salehi, Journal of Materials Science: Materials in Electronics 33, 25153 (2022); https://doi.org/10.1007/s10854-022-09220-7

[24] Y. Sun, W. Yue, B. Niu, Y. Lin, X. Liu, T. Wu, G. Zhang, K. Qu, L. Wang, Y. Niu, Journal of Materials Chemistry B 11, 3434 (2023); https://doi.org/10.1039/D3TB00245D

[25] M. Mahmoodabadi, M. T. Goodarzi, N. Salehi, A. Jalali, E. Zahedi, Applied Physics A 131, 81 (2025); https://doi.org/10.1007/s00339-024-08202-2

[26] T. Mao, Q. Ding, Q. Shan, X. Chang, W. Wu, Advanced Powder Technology 34, 104041 (2023); https://doi.org/10.1016/j.apt.2023.104041

[27] L. Gao, X. Xu, W. Liu, J. Xie, H. Zhang, S. Du, Microchimica Acta 189, 475 (2022); https://doi.org/10.1007/s00604-022-05560-7

[28] L. Geng, J. Sun, M. Liu, J. Huang, J. Dong, Z. Guo, Y. Guo, X. Sun, Food Chemistry 437, 137933 (2024); https://doi.org/10.1016/j.foodchem.2023.137933

[29] M. Xie, F. Zhao, Y. Zhang, Y. Xiong, S. Han, Food Control 131, 108399 (2022); https://doi.org/10.1016/j.foodcont.2021.108399

[30] L. He, R. Huang, P. Xiao, Y. Liu, L. Jin, H. Liu, S. Li, Y. Deng, Z. Chen, Z. Li, N. He, Chinese Chemical Letters 32, 1593 (2021); https://doi.org/10.1016/j.cclet.2020.12.054

[31] P. Wei, S. Wang, W. Wang, Z. Niu, A. Rodas-Gonzalez, K. Li, L. Li, Q. Yang, Applied Surface Science 604, 154369 (2022); https://doi.org/10.1016/j.apsusc.2022.154369

[32] J. Pan, W. Xu, W. Li, S. Chen, Y. Dai, S. Yu, Q. Zhou, F. Xia, Analytical Chemistry 95, 420 (2023); https://doi.org/10.1021/acs.analchem.2c04498

[33] J. C. Abrego-Martinez, M. Jafari, S. Chergui, C. Pavel, D. Che, M. Siaj, Biosensors and Bioelectronics 195, 113595 (2022); https://doi.org/10.1016/j.bios.2021.113595

[34] K. K. Leung, A. M. Downs, G. Ortega, M. Kurnik, K. W. Plaxco, ACS Sensors 6, 3340 (2021); https://doi.org/10.1021/acssensors.1c01183

[35] A. M. Downs, J. Gerson, K. K. Leung, K. M. Honeywell, T. Kippin, K. W. Plaxco, Scientific Reports 12, 5535 (2022); https://doi.org/10.1038/s41598-022-09070-7

[36] H. Liu, S. Ma, G. Ning, R. Zhang, H. Liang, F. Liu, L. Xiao, L. Guo, Y. Zhang, C.-P. Li, H. Zhao, Talanta 258, 124433 (2023); https://doi.org/10.1016/j.talanta.2023.124433

[37] E. Rahbarimehr, H. P. Chao, Z. R. Churcher, S. Slavkovic, Y. A. Kaiyum, P. E. Johnson, P.

Dauphin-Ducharme, Analytical Chemistry 95, 2229 (2023); https://doi.org/10.1021/acs.analchem.2c03566

[38] S. Li, J. Dai, M. Zhu, N. Arroyo-Currás, H. Li, Y. Wang, Q. Wang, X. Lou, T. E. Kippin, S. Wang, K. W. Plaxco, H. Li, F. Xia, ACS Nano 17, 18525 (2023); https://doi.org/10.1021/acsnano.3c06520

39. J. Chung, L. Sepunaru, K. W. Plaxco, ECS Sensors Plus 1, 011604 (2022); https://doi.org/10.1149/2754-2726/ac60b2